symmetry

Article

A Free Convective Two-Phase Flow of Optically Thick Radiative Ternary Hybrid Nanofluid in an Inclined Symmetrical Channel through a Porous Medium

K. M. Pavithra [1,†], Pudhari Srilatha [2], B. N. Hanumagowda [1], S. V. K. Varma [1], Amit Verma [3], Shalan Alkarni [4] and Nehad Ali Shah [5,*,†]

1 Department of Mathematics, School of Applied Sciences, REVA University, Bengaluru 560064, Karnataka, India; r21pmt06@reva.edu.in (K.M.P.); hanumagowda.bn@reva.edu.in (B.N.H.); vijayakumar.varma@reva.edu.in (S.V.K.V.)
2 Department of Mathematics, Institute of Aeronautical Engineering, Hyderabad 500043, Telangana, India; p.srilatha@iare.ac.in
3 Department of Computer Science & Engineering, University Centre for Research & Development, Chandigarh University, Mohali 140413, Punjab, India; amit.e9679@cumail.in
4 Department of Mathematics, College of Sciences, King Saud University, P.O. Box 2455, Riyadh 11451, Saudi Arabia; shalkarni@ksu.edu.sa
5 Department of Mechanical Engineering, Sejong University, Seoul 05006, Republic of Korea
* Correspondence: nehadali199@sejong.ac.kr
† These authors contributed equally to this work and are co-first authors.

Abstract: In the present article, we investigate the free convective flow of a ternary hybrid nanofluid in a two-phase inclined channel saturated with a porous medium. The flow has been propelled using the pressure gradient, thermal radiation, and buoyancy force. The flow model's governing equations are resolved using the regular perturbation approach. The governing equations are solved with the help of the regular perturbation method. Polyethylene glycol and water (at a ratio of 50%:50%) fill up Region I, while a ternary hybrid nanofluid based on zirconium dioxide, magnesium oxide, and carbon nanotubes occupies Region II. The ternary hybrid nanofluids are defined with a mixture model in which three different shapes of nanoparticles, namely spherical, platelet, and cylindrical, are incorporated. The consequences of the most significant variables have been examined using both visual and tabular data. The main finding of this work is that utilising a ternary hybrid nanofluid at the plate y = 1 increases the rate of heat transfers by 753%, demonstrating the potential thermal efficiency. The overall heat and volume flow rates are amplified by buoyant forces and viscous dissipations and dampened by the thermal radiation parameter. The optimum enhancement of temperature is achieved by the influence of buoyancy forces. A ternary nanofluid region experiences the maximum temperature increase compared to a clear fluid region. To ensure the study's efficiency, we validated it with prior studies.

Keywords: carbon nanotube; shape factor; viscous and Darcy dissipation; ternary hybrid nanofluids; thermal radiation; porous medium

Citation: Pavithra, K.M.; Srilatha, P.; Hanumagowda, B.N.; Varma, S.V.K.; Verma, A.; Alkarni, S.; Shah, N.A. A Free Convective Two-Phase Flow of Optically Thick Radiative Ternary Hybrid Nanofluid in an Inclined Symmetrical Channel through a Porous Medium. *Symmetry* **2023**, *15*, 1615. https://doi.org/10.3390/sym15081615

Academic Editor: Iver H. Brevik

Received: 25 July 2023
Revised: 10 August 2023
Accepted: 16 August 2023
Published: 21 August 2023

1. Introduction

Fluid mechanics uses the fundamental principles of thermodynamics and mechanics to explain the motion of fluids. The laws of fluid dynamics govern every aspect of our natural and technological surroundings. Life on Earth would not be sustainable, nor would the technical processes be able to function without fluid flows. We rely entirely on fluid dynamics to produce a wide range of products that are essential to the high standard of living we enjoy today. Many industries use heat transfer fluids as heat carriers, including the heating and cooling industries. Examples: petrochemical, textile, transportation industries, etc. The efficiency of these systems is significantly influenced by the fluid's thermal conductance. As metals have better thermal conductivity compared to fluids, there is no doubt that metallic liquids conduct heat better than conventional heat transfer fluids. Incorporating metallic particles into conventional heat transfer fluids is a standard way to achieve high efficiency. As a result, a new class of artificial fluid called nanofluid came into existence. These are prepared by dispersing nanometer-sized particles into base fluids. Nanofluid was first defined by Choi and Eastman [1]. Further, they noticed that nanofluids have superior thermophysical properties compared to base fluids. Several factors influence nanofluids' heat conduction, including the geometry, stability, size, and type of base fluid. Furthermore, some of the necessary properties required for particular applications are lacking in nanofluids. Hybrid nanofluids have been introduced to obtain increased qualities suitable for applications requiring outstanding thermal, optical, and rheological features of the heat transfer fluid. It has become increasingly apparent that hybrid nanofluids are more effective than ordinary heat transfer fluids due to their improved thermophysical characteristics. Two pioneering studies of hybrid nanofluids were conducted by Turcu et al. [2] and Jana et al. [3]. Then, Suresh et al. [4] investigated the experimental process for manufacturing hybrid copper and aluminum oxide nanofluids. The authors found that, compared to deionized water, hybrid nanofluids had a considerably higher thermal conductivity. There are many shapes available that can be used in industries as well as in drug delivery. However, in recent years, carbon nanotubes have gained researchers' attention because of their outstanding mechanical strength and thermal conductivity. And also, the thermal conductivity of CNTs (carbon nanotubes) can be altered by changing length and diameter according to applications. CNTs are extensively used in applications such as automotive parts, energy storage, thin-film electronics, electromagnetic shields, etc.

The simultaneous flow of multiple phases is known as multiphase flow. Multiphase flow research is becoming ever more important in energy-related industries and applications. However, two-phase flow is the simplest form of multiphase flow and is extensively used in liquid extraction systems. Investigating the motion of Newtonian fluids in a two-layer conduit, Chen and Jian [5] found some interesting results. The authors noticed that the flow parameters influence the total entropy generation. The flow of distinct Maxwell fluids in an indefinitely extending horizontal two-phase channel was examined by Hisham et al. [6]. The findings showed that the fluid reaches its maximum velocity when $y = 1$. Yadav and Kumar [7] investigated the flow of Newtonian and micropolar fluids in a two-phase conduit subjected to a magnetic field. The authors observed that the linear and microrotational velocities are reduced by an increase in the Hartmann number. The interruption of a viscous fluid's steady flow in a diverging channel brought on by heat radiation and a magnetic field with slip was investigated by Mallikarjuna et al. [8]. The results show that as the Prandtl number rises, so does the temperature of the fluid.

Moreover, porous materials can be found in almost every aspect of our lives, from daily life to technology. In other words, fluid flow through a porous medium is affected by specific surface area, strong surface effect, viscous effect, fluid compressibility, and molecular force. Research into porous media is growing in prominence due to its numerous possible uses in the engineering and scientific fields. In a porous channel subjected to an applied magnetic field, carbon nanotubes (CNTs) were studied by Zeeshan et al. [9] in the context of two-layer nanofluid flow. The thickness of the thermal boundary layer was shown to have a linear relationship with the solid volume fraction of CNT. The steady laminar flow of fluid in a uniformly porous rectangular duct was examined by Umavathi and Beg [10]. In order to increase skin friction at the walls, the scientists found that thermal buoyancy and porosity parameters were beneficial.

The unsteady flow of squeezed nanofluid via parallel discs was studied by Dogonchi et al. [11]. It was discovered that both the injection and suction parameters directly impact heat transmission. The unsteady upward flow of hybrid nanofluids between two concentric cylinders was studied by Rahim et al. [12]. According to the authors, the porosity parameter decreases temperature while the magnetic field decreases velocity. Yaseen et al. [13] examined the flow of a hybrid nanofluid through a porous medium enclosed by parallel plates that was subjected to a magnetic field. The authors observed that nanofluids do not tend to transfer heat at the same rate as hybrid nanofluids. Pattnaik et al. [14] looked at the effect of a stretched sheet on its shape parameters and the heat radiation of a nanofluid flowing across the sheet. According to the authors, skin friction increases with a rise in the value of the magnetic parameter and volume fraction of a nanoparticle.

The axisymmetric flow of a hybrid nanofluid through a vertical cylinder filled with porous media was investigated by Khan et al. [15]. The findings showed that the radiation and curvature parameters both increased the drag force. Upreti et al. [16] studied CNTs' impact on hybrid nanofluids between two rotating parallel plates along an axis perpendicular to the plates' plane of motion. Their analysis determined that a higher volume fraction of CNT increased hybrid nanofluids thermal conductivity compared with nanofluids.

Masood and Farooq [17] studied the motion of a hybrid nanofluid through a stretched sheet while subjected to thermal radiation and stratification. According to the authors, heat transfer rates decrease as radiation and stratification parameters increase. A fluid's two-phase flow in an infinite channel was studied by Xiong et al. [18]. According to the findings, the rate of flow and temperature both increased as the values of the couple stress parameters increased. The impact of heat radiation on the flow of a Hafnium-Jeffrey nanofluid across a porous medium was examined by Ge-Jile et al. [19]. It has been observed that the Brinkman number enhances the temperature in all types of flows.

Wakif et al. [20] looked into the impact of heat radiation on a Couette nanofluid flow in an infinite vertical conduit subjected to a magnetic field. The Brownian, thermal radiation, and thermophoresis parameters were found to increase fluid temperature. The solar collector absorbing solar radiation was modelled using a hybrid nanofluid as a base fluid by Xiong et al. [21]. It was discovered that low Reynolds numbers are necessary to reach the maximum supply temperature.

In the presence of mass diffusion and spin effects, Al-Hossainy and Eid [22,23] investigated the behaviour of a PEG(Polyethylene glycol)-based hybrid nanofluid as it moved through thin films and parallel plates. They found that elevating the volume fraction of solids reduces the fluid's temperature and concentration. Babu et al. [24] looked into the behaviour of hybrid nanofluid across a magnetised sensor surface and looked into the impact of radiation and viscosity dissipation. The authors discovered that the squeezed flow index parameter has a strong inverse relationship with surface drag force.

Murshid et al. [25] investigated the effects of constant pressure and a heat source on the unsteady movement of hybrid nanofluid in a conduit. It was discovered that raising the radiation parameter led to a decrease in the fluid's temperature. For their study, Ahmad and Nadeem [26] employed nonlinear thermal convection to examine the movement of a dusty-micropolar hybrid nanofluid across a stretched sheet. The authors discovered that nanofluids outperform dusty fluids in terms of fluid temperature enhancement. Rana et al. [27] inquired about the effect that non-linear heat radiation has on the axis-symmetric flow of a hybrid nanofluid through a rotating cylinder. The findings showed that despite changes in radiation parameters, the Nusselt number remained positive.

"Ternary hybrid nanofluids" are fluids containing three different combinations of nanoparticles. Many scientific fields are set to benefit from the newly created ternary hybrid nanofluids with variously shaped nanoparticles [28]. The effectiveness of ternary nanofluids is highly dependent on nanoparticle type, size, and concentration.

In their study, Shamshuddin et al. [29] analysed the behaviour of a ternary hybrid nanofluid as it flowed across a spinning disc heated by radiation and influenced by the Hall parameters. In contrast to nano and hybrid nanofluids, the authors found that ternary nanofluids have an enhanced rate of heat transmission. Obai Younis et al. [30] explored the thermal storage of phase transition material in an undulated channel in the heat exchanger. Abderrahmane et al. [31] investigated the non-Newtonian nanofluid's natural convection. In a rotating channel, the confined flow of CNT nanofluid was studied by researchers Ghadikolaei et al. [32]. The researchers discovered that the horizontal linear velocity is affected by changes in the value of the rotational parameter. Pavithra et al. [33,34] studied the heat radiation behaviour inside an inclined channel. The researchers found that fluid temperature rises as the Grashof number increases and that the shape of lamina nanoparticles can demonstrate maximal enhancement in heat transfer as compared to other shapes.

Sarada et al. [35] examined the performance of base fluid by adding trio nanoparticles to a curved stretching sheet. They discovered that the Biot and Schmidt numbers have opposing effects on heat and mass transmission. Billal et al. [36] investigated the performance of ternary hybrid nanofluids in a conduit. The trio hybrid nanofluids in a square cavity were analysed by Sahoo [37] and Sahu and Sarkar [38]. Arif et al. [39] conducted a heat transfer analysis of differently shaped nanoparticles in a single base fluid between two parallel plates. Ternary hybrid nanofluids improve heat transport by 33.67%, as determined by the authors.

ZrO_2 (Zirconium dioxide) and MgO (Magnesium oxide) have advanced significantly in a wide range of applications due to their superior heat and corrosion resistance. Considering that MgO and ZrO_2 have comparable thermal properties, they are often mixed. It is challenging to move heat through MgO because of its poor thermal conductivity. The strong stability of ZrO_2 at low temperatures, on the other hand, makes it ideal for applications that need high temperatures. Combining the two substances allows for the production of materials that are stable in both mechanical and thermal environments [40].

The aforementioned studies focused on the interaction of ternary hybrid nanofluids, hybrid nanofluids, and nanofluids between two parallel plates. The two-phase flow of transparent and ternary hybrid nanofluids with various nanoparticle morphologies in the presence of radiation has not, as far as the author is aware, been studied. However, the following distinguishes our work from past research studies.

(i) The two-phase flow of ternary hybrid nanofluids with various nanoparticle morphologies with viscous dissipation and natural convection.
(ii) The effect of thermal radiation on porous medium is incorporated.
(iii) In order to increase heat transfer, we used PEG water (50%:50%) containing spherical ZrO_2 nanoparticles, platelet-shaped MgO nanoparticles, and CNTs.

As a result, we intend to test the efficiency of nanoparticles in enhancing heat transfer potential in PEG–water-based hybrid nanofluids using the aforementioned nanoparticles and CNTs. Table 1 illustrates the thermophysical properties of the base fluids and nanoparticles.

Table 1. Thermophysical properties [22,41].

	k(W/mk)	**ρ(kg/m^3)**	**β(/K)**
PEG–Water (50%:50%)	0.3712	1110	5.8×10^{-4}
ZrO_2	1.7	5680	10×10^{-6}
MgO	45	3560	1.05×10^{-5}
SWCNT	2000	2200	1.5×10^{-5}

2. Mathematical Formulation

The flow geometry of the problem is visualized in Figure 1. PEG–water (50%:50%) is present in the first region $(-h \leq y \leq 0)$, while a ternary hybrid nanofluid (PEG–water-based) is present in the second region $(0 \leq y \leq h)$ and is in contact with a porous medium. The plates are maintained at a constant temperature such that the temperature of the plate $y = -1$ is T_{w2} and that of the plate $y = 1$ is T_{w1}, with the condition that $T_{w1} > T_{w2}$, which are inclined at an angle ψ horizontal to the axis. Assumptions include that the flow is steady, laminar, incompressible, mixed convective, and parallel to the x-axis. Fluids having constant thermophysical properties aside from density in the buoyancy term are taken into consideration. The effects of thermal radiation, viscous, and Darcy dissipation are incorporated. Ternary hybrid nanofluids are described with mixture model [42] expressions based on the Tiwari and Das model [43]. Constant pressure gradients and viscous forces drive the flow. The Oberbeck-Boussinesq approach results in the governing equations for two-phase flow by assuming a constant pressure gradient along the channel length. Moreover, we assume that the interface has a continuous temperature, velocity, shear stress, and heat flux.

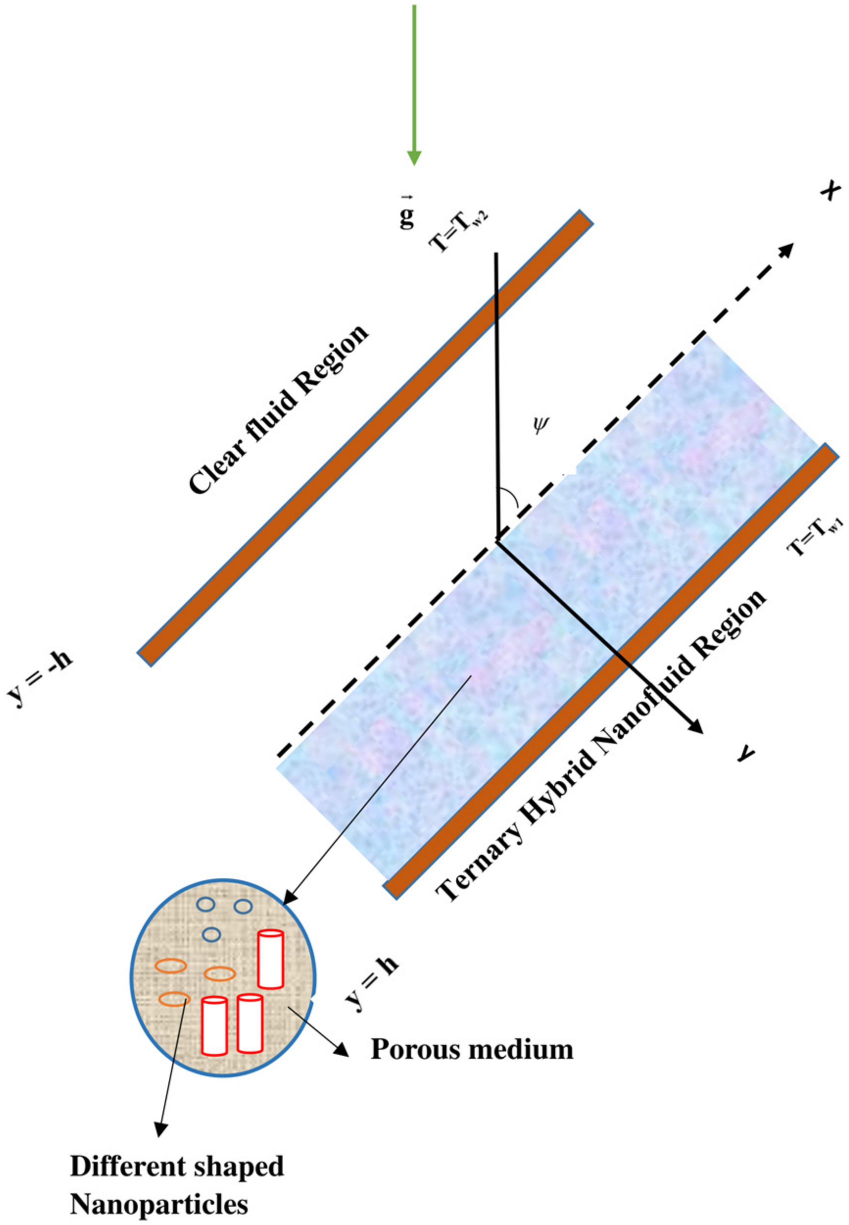

Figure 1. Flow geometry.

2.1. Governing Equations

Region-I

$$\mu_f \frac{d^2 u'_1}{dy'^2} + \left(\rho_f g \beta_f\right)(T_1 - T_{w2})\cos(\psi) - \frac{\partial p}{\partial x} = 0 \quad (1)$$

$$k_f \frac{d^2 T_1}{dy'^2} + \mu_f \left(\frac{du'_1}{dy'}\right)^2_1 - \frac{\partial q_r}{\partial y} = 0 \quad (2)$$

Region-II

$$\mu_{thnf}\frac{d^2u'_2}{dy'^2}+\left(\rho_{thnf}g\beta_{thnf}\right)(T_2-T_{w2})\cos(\psi)-\frac{\mu_{thnf}}{K}u'_2-\frac{\partial p}{\partial x}=0 \tag{3}$$

$$k_{thnf}\frac{d^2T_2}{dy'^2}+\mu_{thnf}\left(\frac{du'_2}{dy'}\right)^2+\frac{\mu_{thnf}}{K}u'_2{}^2-\frac{\partial q_r}{\partial y}=0 \tag{4}$$

Boundary and interface conditions as implemented are

$$\left.\begin{array}{c} u'_1(-h)=0, u'_1(0)=u'_2(0), \mu_f\frac{du'_1(0)}{dy'}=\mu_{thnf}\frac{du'_2(0)}{dy'},\ u'_2(h)=0 \\ T_1(-h)=T_{w2},\ T_1(0)=T_2(0),\ k_f\frac{dT_1(0)}{dy'}=k_{thnf}\frac{dT_2(0)}{dy'},\ T_2(h)=T_{w1} \end{array}\right\} \tag{5}$$

Additionally, we assessed the effect of nanoparticles with spherical, platelet, and cylindrical shapes on the base fluid's capacity to transfer heat. The thermophysical properties of nanoparticles and base fluids are calculated using a mixture model [42].

2.2. Thermophysical Properties

$$\text{Density}\quad \rho_{hnf}=(1-\phi_1-\phi_2-\phi_3)\rho_{bf}+\phi_1\rho_1+\phi_2\rho_2+\phi_3\rho_3 \tag{6}$$

Specific Heat

$$\left(\rho C_p\right)_{hnf}=\left(\rho C_p\right)_{bf}(1-\phi_1-\phi_2-\phi_3)+\left(\rho C_p\right)_1\phi_1+\left(\rho C_p\right)_2\phi_2+\left(\rho C_p\right)_3\phi_3 \tag{7}$$

Coefficient of thermal expansion

$$(\rho\beta_T)_{hnf}=(1-\phi_1-\phi_2-\phi_3)(\rho\beta_T)_{bf}+\phi_1(\rho\beta_T)_1+\phi_2(\rho\beta_T)_2+\phi_3(\rho\beta_T)_3 \tag{8}$$

Maxwell Garnett model [42]
Thermal conductivity

$$k_{nf}=k_{bf}\left(\frac{k_p+(m-1)k_f+(m-1)\phi\left(k_p-k_f\right)}{k_p+(m-1)k_f-\phi\left(k_p-k_f\right)}\right) \tag{9}$$

For spherical nanoparticles-ZrO_2

$$k_{nf1}=k_{bf}\left(\frac{k_1+(3-1)k_f+(3-1)\phi_1\left(k_1-k_f\right)}{k_1+(3-1)k_f-\phi_1\left(k_1-k_f\right)}\right) \tag{10}$$

For platelet -shaped nanoparticle-MgO

$$k_{nf2}=k_{bf}\left(\frac{k_2+4.7k_f+4.7\phi_2\left(k_2-k_f\right)}{k_2+4.7k_f-\phi_2\left(k_2-k_f\right)}\right) \tag{11}$$

For cylindrical-shaped nanoparticle-SWCNT

$$k_{nf3}=k_{bf}\left(\frac{k_3+3.9k_f+3.9\phi_3\left(k_3-k_f\right)}{k_3+3.9k_f-\phi_3\left(k_3-k_f\right)}\right) \tag{12}$$

Viscosity in terms of the Einstein–Batchelor equation [44,45]
For spherical nanoparticles -ZrO_2

$$\mu_{nf1}=\mu_f\left(1+2.5\phi_1+6.2\phi_1^2\right) \tag{13}$$

For platelet-shaped nanoparticle-MgO

$$\mu_{nf2} = \mu_f \left(1 + 37.1\phi_2 + 612.6\phi_2^2\right) \tag{14}$$

For cylindrical-shaped nanoparticle-SWCNT

$$\mu_{nf3} = \mu_f \left(1 + 13.5\phi_3 + 904.4\phi_3^2\right) \tag{15}$$

Dynamic viscosity of ternary hybrid nanofluid.

$$\mu_{hnf} = \mu_{nf1} \times \phi_1 + \mu_{nf2} \times \phi_2 + \mu_{nf3} \times \phi_3 \tag{16}$$

Effective thermal conductivity of ternary hybrid nanofluid

$$k_{hnf} = \frac{k_{nf1}\phi_1 + k_{nf2}\phi_2 + k_{nf3}\phi_3}{\phi_{hnf}} \tag{17}$$

where $\phi_{hnf} = \phi_1 + \phi_2 + \phi_3$.

Rosseland's estimate [46] provides the formula for the radiant heat flux [47] in the direction of y'

$$q_r = -\frac{4\sigma_s}{3k_a}\frac{\partial}{\partial y\prime}\left(T^4\right) \tag{18}$$

The scope of the current analysis is restricted to optically thick fluids as a result of the Rosseland approximation's application. If the temperature changes within the flow are modest enough, expanding T^4 into the Taylor series about T_∞ while ignoring higher-order variables allows us to construct a linear form of Equation (13) as shown below.

$$T^4 = 4\left(T_\infty^3 T\right) - 3T_\infty^4 \tag{19}$$

Further, the term $\frac{\partial q_r}{\partial y\prime}$ in (2) and (4) will become

$$\frac{\partial q_r}{\partial y\prime} = -\frac{16}{3}\left(\frac{\sigma_s T_\infty^3}{k_a}\right)\frac{\partial^2 T}{\partial y\prime^2} \tag{20}$$

Since ternary hybrid nanofluid is composed of spherical, platelet-shaped, and cylindrical nanoparticles, Table 2 displays the relevant sphericity and shape parameters.

Table 2. Values of sphericity and shape factor [39].

Shape	Spherical	Platelets	Cylindrical
Sphericity (η)	1	0.52	0.612
Shape factor (m)	3	5.7	4.9

2.3. Non-Dimensional Parameters for Region-I and II

$$y = \frac{y'}{h},\ u_i = u'_i\left(\frac{\rho_f}{\mu_f}\right)h,\ \theta_i = \frac{T_i - T_{w2}}{T_{w1} - T_{w2}},\ G_{r1} = \frac{g\beta_f(T_{w1} - T_{w2})h^3}{v_f^2},$$

$$Grt = G_{r1}\mathrm{Cos}(\gamma),\ Br = \frac{\mu_f^3}{\rho_f^2 h^2(T_{w1} - T_{w2})k_f}\sigma = \frac{h}{\sqrt{K}},\ P = -\frac{\rho_f h^3}{\mu_f^2}\frac{\partial p}{\partial x},$$

$$v_f = \frac{\mu_f}{\rho_f},\ R = \frac{16\sigma_s T_\infty^3}{3K_a k_f} \tag{21}$$

Upon substituting above-mentioned dimensionless parameters into Equations (1)–(5), we get

Region-I

$$\frac{d^2u_1}{d^2y} + (Grt\theta_1) + P = 0 \tag{22}$$

$$N_1\frac{d^2\theta_1}{dy^2} + Br\left\{\left(\frac{du_1}{dy}\right)^2\right\} = 0 \tag{23}$$

Region-II

$$\frac{d^2u_2}{dy^2} + aGrt\theta_2 - \sigma^2u_2 + P_1 = 0 \tag{24}$$

$$N_2\frac{d^2\theta_2}{dy^2} + Brc\left[\left(\frac{du_2}{dy}\right)^2 + \sigma^2u_2^2\right] = 0 \tag{25}$$

For Region-I and Region-II, these are the boundary and interface conditions:

$$\begin{array}{ll} At \quad y=-1 & \left.\begin{array}{c} u_1 = 0 \\ \theta_1 = 0 \end{array}\right\} \\ At \quad y=0 & \left.\begin{array}{c} u_1 = u_2 \\ \theta_1 = \theta_2 \end{array}\right\} \\ At \quad y=0 & \left.\begin{array}{c} \frac{du_1}{dy} = \frac{\mu_{thnf}}{\mu_f}\frac{du_2}{dy} \\ \frac{d\theta_1}{dy} = \frac{k_{thnf}}{k_f}\frac{d\theta_2}{dy} \end{array}\right\} \\ At \quad y=1 & \left.\begin{array}{c} u_2 = 0 \\ \theta_2 = 1 \end{array}\right\} \end{array} \tag{26}$$

3. Method of Solution

The nature of the transport Equations (22)–(26) are non-linear where exact analytical solutions are not possible. Therefore, by employing the Regular perturbation technique, the approximate solution for temperature and velocity is obtained. The perturbation parameter considered here is the Brinkmann number.

$$\left.\begin{array}{l} u_i = u_{i0} + Bru_{i1} + Br^2u_{i2} + \ldots \\ \theta_i = \theta_{i0} + Br\theta_{i1} + Br^2\theta_{i2} + \ldots \end{array}\right\} \tag{27}$$

Upon substituting (22)–(26) in (27) and equating equal powers of the Brinkmann number to zero, we get following equations.

Region-I

Zeroth order

$$\frac{d^2u_{10}}{dy^2} + (Grt\theta_{10}) + P = 0 \tag{28}$$

$$\frac{d^2\theta_{10}}{dy^2} = 0 \tag{29}$$

First order

$$\frac{d^2u_{11}}{d^2y} + (aGrt\theta_{11}) = 0 \tag{30}$$

$$N_1\frac{d^2\theta_{11}}{dy^2} + \left\{\left(\frac{du_{10}}{dy}\right)^2\right\} = 0 \tag{31}$$

Region-II

Zeroth order

$$\frac{d^2u_{20}}{dy^2} + aGrt\theta_{20} - \sigma^2u_{20} + P_1 = 0 \tag{32}$$

$$\frac{d^2\theta_{20}}{dy^2} = 0 \tag{33}$$

First order

$$\frac{d^2u_{21}}{dy^2} + aGrt\theta_{21} - \sigma^2 u_{21} = 0 \tag{34}$$

$$N_2\frac{d^2\theta_{21}}{dy^2} + c\left[\left(\frac{du_{20}}{dy}\right)^2 + \sigma^2 u_{20}^2\right] = 0 \tag{35}$$

For the zeroth and first order, conditions at the boundary and interface are

$$\left.\begin{array}{l} u_{10}(-1) = 0, u_{10}(0) = u_{20}, \mu_f \frac{du_{10}}{dy}(0) = \mu_{thnf}\frac{du_{20}}{dy}(0), u_{20}(1) = 0 \\ \theta_{10}(-1) = 0, \theta_{10}(0) = \theta_{20}(0), k_f\frac{d\theta_{10}}{dy}(0) = k_{thnf}\frac{d\theta_{20}}{dy}(0), \theta_{20}(1) = 1 \end{array}\right\} \tag{36}$$

$$\left.\begin{array}{l} u_{11}(-1) = 0, u_{11}(0) = u_{21}(0), \mu_f \frac{du_{11}}{dy}(0) = \mu_{thnf}\frac{du_{21}}{dy}(0), u_{21}(1) = 0 \\ \theta_{11}(-1) = 0, \theta_{11}(0) = \theta_{21}(0), k_f\frac{d\theta_{11}}{dy}(0) = k_{thnf}\frac{d\theta_{21}}{dy}(0), \theta_{21}(1) = 1 \end{array}\right\} \tag{37}$$

where, u_i, θ_i $(i = 1, 2)$ are functions of y.

The zeroth and first order solutions for the distributions of temperature and velocity are

Temperature distribution

$$\theta_{10} = b_1 y + b_2 \tag{38}$$

$$\theta_{20} = b_3 y + b_4 \tag{39}$$

$$\theta_{11} = -\frac{1}{N_1}\left(L_5y^6 + L_6y^5 + L_7y^4 + L_8y^3 + L_9y^2\right) + c_{31}y + c_{32} \tag{40}$$

$$\theta_{21} = \frac{-c}{N_2}\left(\begin{array}{c} L_{20}\cosh 2\sigma y + L_{21}\text{sinh}2\sigma y + L_{22}y\cosh\sigma y + L_{23}y\text{sinh}\sigma y \\ +L_{24}\cosh\sigma y + L_{25}\text{sinh}\sigma y + L_{26}y^4 + L_{27}y^3 + L_{28}y^2 \end{array}\right) + c_{41}y + c_{42} \tag{41}$$

Velocity distribution

$$u_{10} = L_1y^3 + L_2y^2 + c_{11}y + c_{12} \tag{42}$$

$$u_{20} = c_{21}\cosh\sigma y + c_{22}\text{sinh}\sigma y - \frac{1}{\sigma^2}(L_3y + L_4) \tag{43}$$

$$u_{11} = \frac{aGr}{N_1}\left(L_{37}y^8 + L_{38}y^7 + L_{39}y^6 + L_{40}y^5 + L_{41}y^4 + L_{42}y^3 + L_{43}y^2\right) + c_{51}y + c_{52} \tag{44}$$

$$u_{21} = -aGrt\left(\begin{array}{l} c_{61}\cosh\sigma y + c_{62}\text{sinh}\sigma y + L_{29}\cosh 2\sigma y \\ +L_{30}\text{sinh}2\sigma y + L_{31}y^2\text{sinh}\sigma y - L_{32}y\cosh\sigma y + L_{33}y^2\text{cosh}\sigma y \\ +L_{34}y\text{sinh}\sigma y + L_{35}\text{sinh}\sigma y + L_{36}y\cosh\sigma y \\ -\frac{1}{\sigma^2}\left(L_{26}y^4 + L_{27}y^3 + L_{28}y^2 + \frac{1}{\sigma^2}\left(12L_{26}y^2 + 6L_{27}y + 2L_{28}\right)\right) - \frac{1}{\sigma^2}(c_{31}y + c_{32}) \end{array}\right) \tag{45}$$

where b_1, b_2, b_3, b_4, $L_1, L_2, \ldots .L_{43}$ are constants given in the Appendix A, and $c_{11}, c_{12}, c_{21}, c_{22}$, $c_{31}, c_{32}, c_{41}, c_{42}, c_{51}, c_{52}, c_{61}, c_{62}$ are the constants obtained during integration.

Consequently, the result of the temperature and velocity equation will be

$$\left.\begin{array}{l} \theta_1 = \theta_{10} + Br\theta_{11} \\ \theta_2 = \theta_{20} + Br\theta_{21} \end{array}\right\} \tag{46}$$

$$\left.\begin{array}{l} u_1 = u_{10} + Bru_{11} \\ u_2 = u_{20} + Bru_{21} \end{array}\right\} \tag{47}$$

where, u_i, $\theta_i(i = 1, 2)$ are functions of y.

Physical Quantities

The non-dimensional derived quantities are determined as follows due to engineering understanding.

Nusselt Number:

$$(Nu_1) = \left(\frac{d\theta_1}{dy}\right)_{y=-1}, \; (Nu_2) = \left(\frac{d\theta_2}{dy}\right)_{y=1} \quad (48)$$

Skin Friction coefficient:

$$(Sk_1) = \left(\frac{du_1}{dy}\right)_{y=-1}, \; (Sk_2) = \left(\frac{du_2}{dy}\right)_{y=1} \quad (49)$$

Further,

The dimensionless total volume flow rate can be calculated using

$$Q_{Vol} = Q_{Vol1} + Q_{Vol2} \quad (50)$$

where $Q_{Vol1} = \int_{-1}^{0} u_1 dy$, $Q_{Vol2} = \int_{0}^{1} u_2 dy$.

The dimensionless total heat rate added to the flow is calculated using

$$E = \int_{-1}^{0} u_1\theta_1 dy + \int_{0}^{1} u_2\theta_2 dy \quad (51)$$

4. Results and Discussions

In-depth discussion of ternary hybrid nanofluids' relevance and potential applicability to practical issues is provided in this article. The interaction between three differently shaped nanoparticles and PEG water is examined in this work. We have blended the PEG water with a combination of spherical ZrO_2, platelet-shaped MgO, and SWCNT. In order to completely comprehend the flow model, the solution of temperature and velocity is obtained using the regular perturbation method. Tables and graphs are used to display the data. The thermal Grashof number $(1 \leq Gr \leq 15)$, the Brinkman number $(0 \leq Br \leq 1)$, the radiation parameter, the porosity parameter $(2 \leq \sigma \leq 8)$, and the ϕ_1, ϕ_2, ϕ_3 are the nanoparticle volume fractions of ZrO_2, MgO, and SWCNT, respectively, and were used as non-dimensionalized constraints to supervise the flow. The following values of the non-dimensional parameters are considered for graphs and tables except the varying parameter. In this context, clear fluid denotes PEG–water, ternary hybrid nanofluid denotes PEG–Water + MgO + ZrO_2, and $y = -1$ and $y = 1$ denote the upper and bottom plates, respectively.

$$Grt = 5,\ P = 5,\ \sigma = 4,\ \phi_1 = \phi_2 = \phi_3 = 0.02,\ Br = 0.5, \psi = \pi/6,\ R = 0.6$$

The thermal Grashof number greatly impacts both the temperature and velocity fields, as shown in Figure 2. As Grt increases, the temperature of the fluid rises in both regions. However, temperature enhancement is primarily substantial in the ternary nanofluid region. Although viscosity forces work against natural convection, they become less powerful as Grt increases. Natural convection will therefore start when the Grt is big enough since the buoyancy forces will be stronger than the viscosity forces. As a result, the fluid's temperature increases. The second region is also filled with a ternary hybrid nanofluid, which has a higher thermal conductivity than clear fluid. The ternary hybrid nanofluid area consequently exhibits the highest enhancement. The impact of on the velocity field is shown in Figure 2. While Grt in this case exhibits behaviour akin to that of temperature, it is discovered that velocity is greatest in the region of clear fluid. Because hybrid ternary nanofluid has a high density, it resists flow. As a result, the velocity in the area of clear fluid rises. The results attained are identical to those of Malashetty et al. [48]. The efficiency of the system as a whole can be increased by incorporating natural convection and heat transfer into solar collectors or heat storage devices.

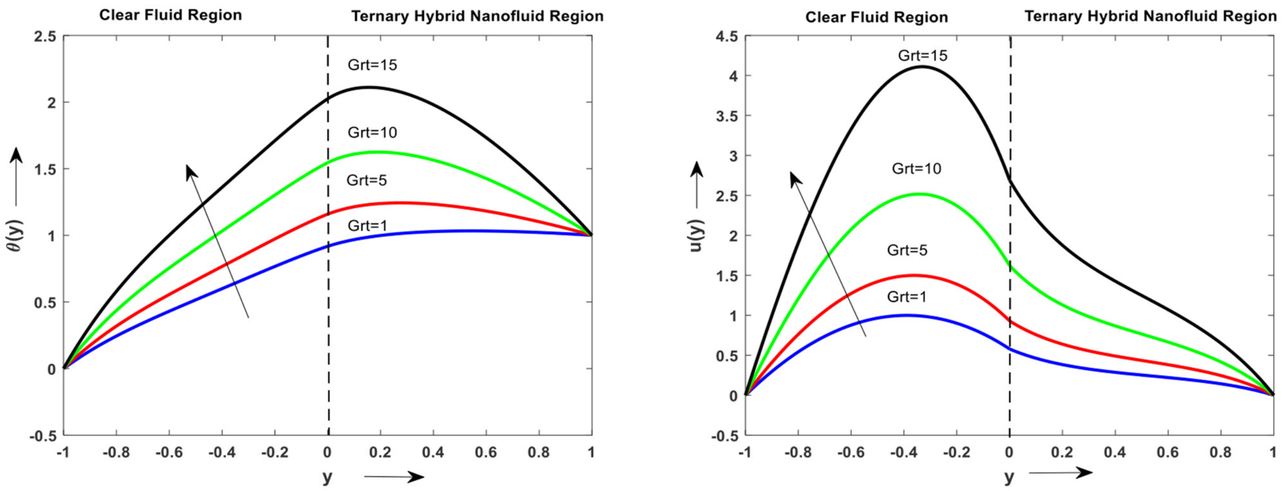

Figure 2. The impact of Grt on $\theta(y)$ and $u(y)$.

As seen in Figure 3, porous media have an impact on temperature and velocity profiles. As σ increases, both regions experience a sudden drop in temperature and fluid velocity. Additionally, the lowering effect has a greater impact in the clear fluid zone for the temperature profile as compared to the ternary nanofluid region. Additionally, the ternary nanofluid zone exhibits a greater reduction in fluid velocity. Complex flow patterns may result from the interaction of the fluid with the porous material. Porous media are frequently used in the oil and gas sector. Optimum oil recovery may be achieved by using porous media with reasonable porosity values, understanding fluid flow, and heat transfer. Similar results have been observed with Umavathi and Hemavathi [49] for all three regions.

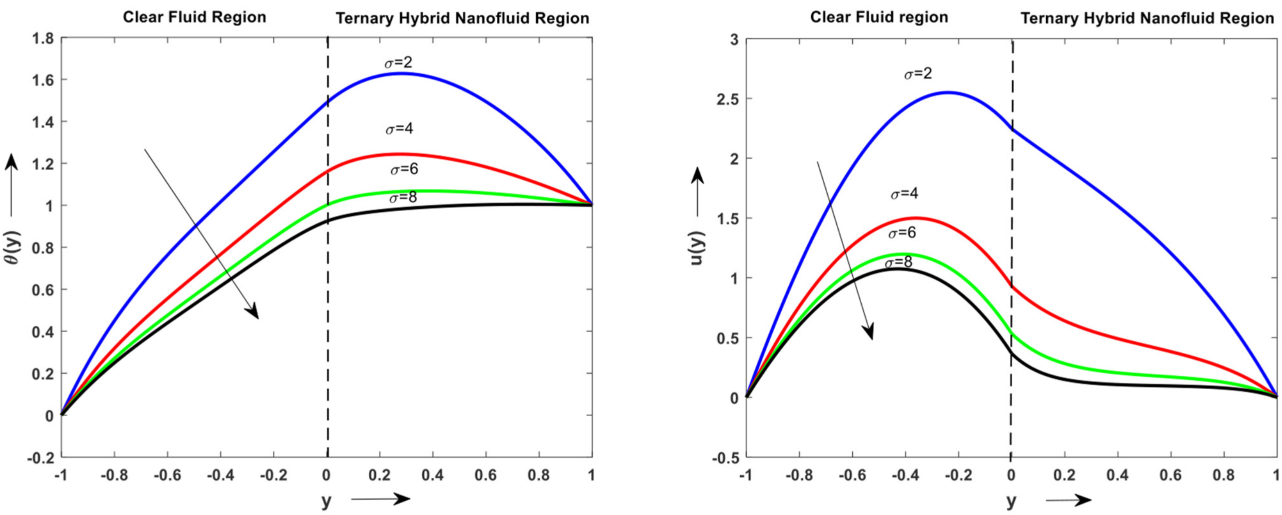

Figure 3. The impact of σ on $\theta(y)$ and $u(y)$.

The impact of Br on temperature and velocity can be viewed in Figure 4. The fluid's temperature rises as Br's value increases. The ternary hybrid nanofluid region exhibits the greatest temperature increase. The capacity of the fluid to transfer heat slows down as Br rises, which enhances the heat generated via viscous dissipation. As a result, the fluid's temperature increases. Furthermore, the impact of Br on the velocity profiles is also shown in Figure 4. In contrast to the ternary hybrid nanofluid region, the clear fluid region has a higher velocity. As Br increases, the viscous dissipation overrides the external heat by conduction. Thus, some kinetic energy in the fluid is converted into thermal energy by its viscosity, which in turn results in an increase in velocity.

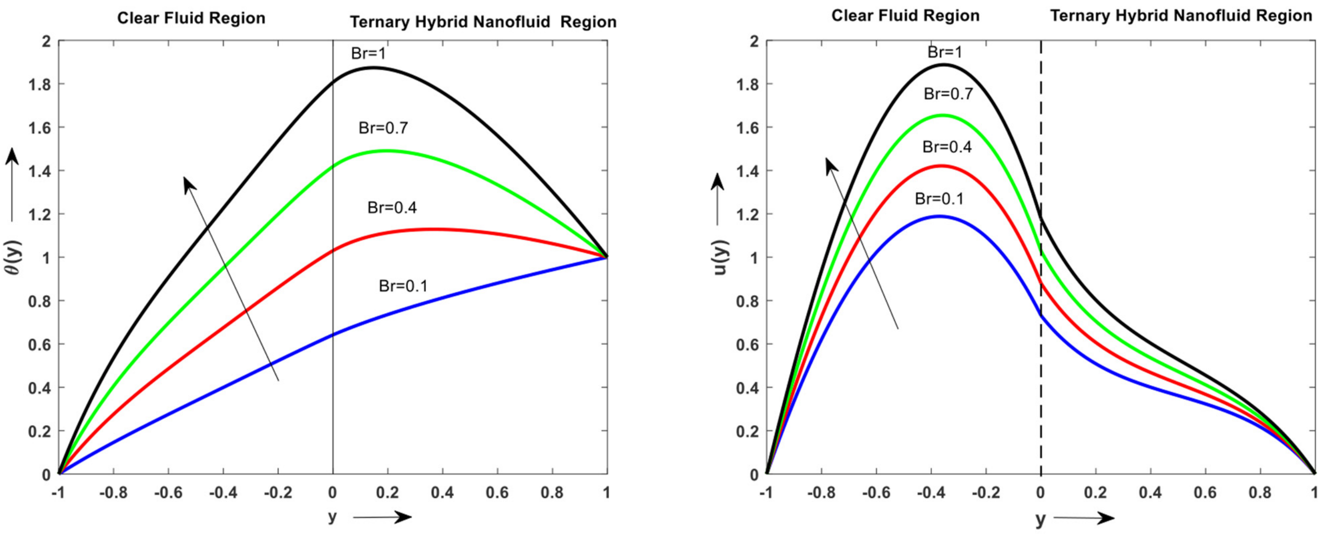

Figure 4. The impact of Br on $\theta(y)$ and $u(y)$.

The consequence of R on temperature and velocity profiles is shown in Figure 5. Increasing R results in a decreasing fluid temperature, as seen in Figure 5. The fluid's temperature is anticipated to drop as radiation slows the rate of energy transfer into the fluid. A similar phenomenon is observed for the velocity profiles depicted in Figure 5. In contrast to the previous observation, the velocity in the region of the ternary nanofluid decreased. The results are in accordance with those of Das et al. [50].

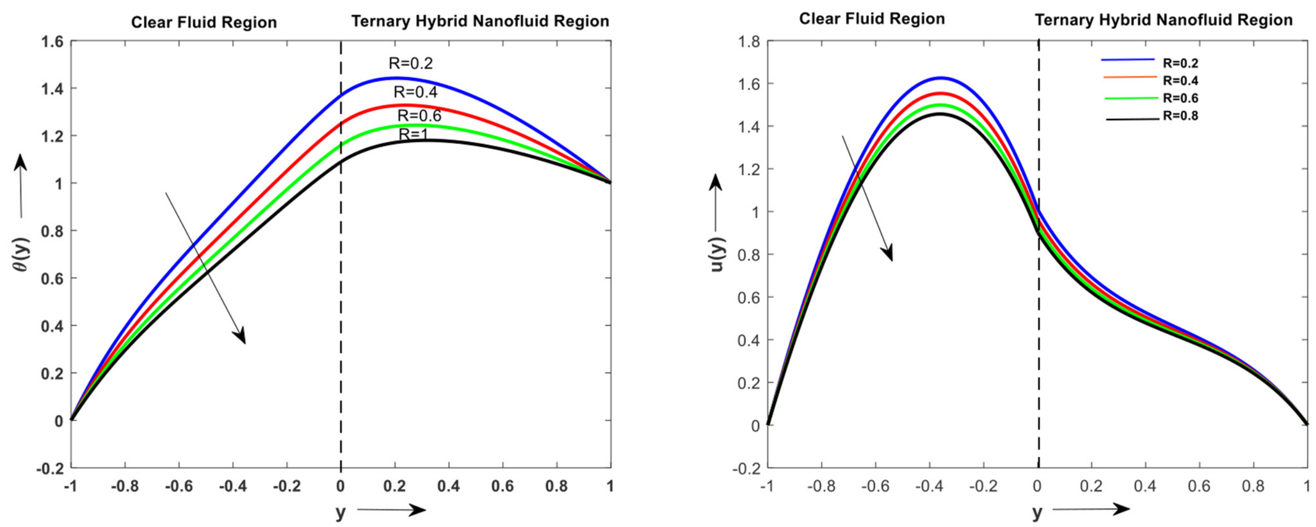

Figure 5. The impact of R on $\theta(y)$ and $u(y)$.

The temperature and velocity profiles are affected by the volume fraction of ZrO_2, as seen in Figure 6. The value of ϕ_1 is varied by considering ϕ_2 and ϕ_3 as constants. Figure 6 makes clear that as ϕ_1 is increased, the fluid's temperature increases. As particle concentrations increase, the fluid's resistive forces also grow, which amplifies kinetic energy and raises the fluid's temperature. The velocity profiles illustrated in Figure 6 exhibit a similar effect. But the velocity of the fluid is relatively high in the clear fluid region.

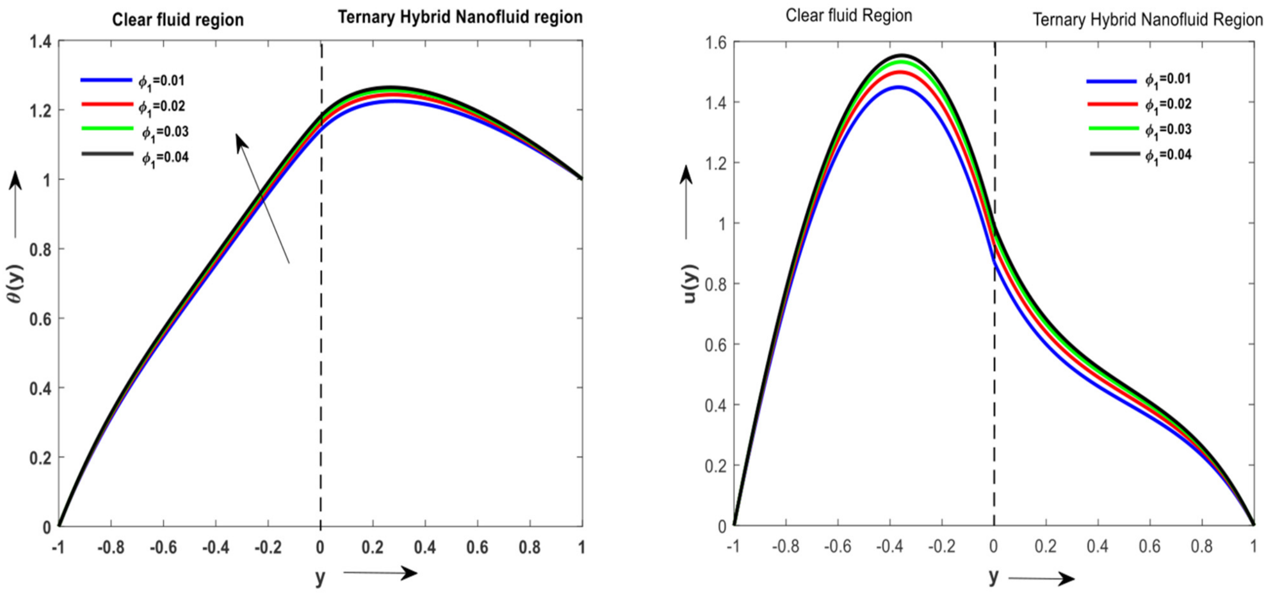

Figure 6. The impact of ϕ_1 on $\theta(y)$ and $u(y)$.

The effects of MgO and SWCNT volume fractions on temperature and velocity are illustrated in Figures 7 and 8. The value of the volume fractions of other nanoparticles is kept constant except for varying ones. In Figure 7, respectively, the effects of ϕ_2 on temperature and velocity are shown. As the solution's MgO concentration rises, the temperature falls. This is because of the material property of MgO, which reduces the fluid's temperature. As shown in Figure 7, the fluid's velocity decreases as the volume fraction of MgO increases. The fluid's temperature and velocity are affected by increasing the volume fraction of SWCNTs, as seen in Figure 8. With escalating ϕ_3 levels, both show a diminishing nature. A possible surface area for heat transfer is provided by the inclusion of various nanoparticle morphologies into the base fluid. In contrast, it stabilises the nanofluid, raising the fluid's temperature. Because of the nature of the substance, a few nanoparticles may have a cooling effect.

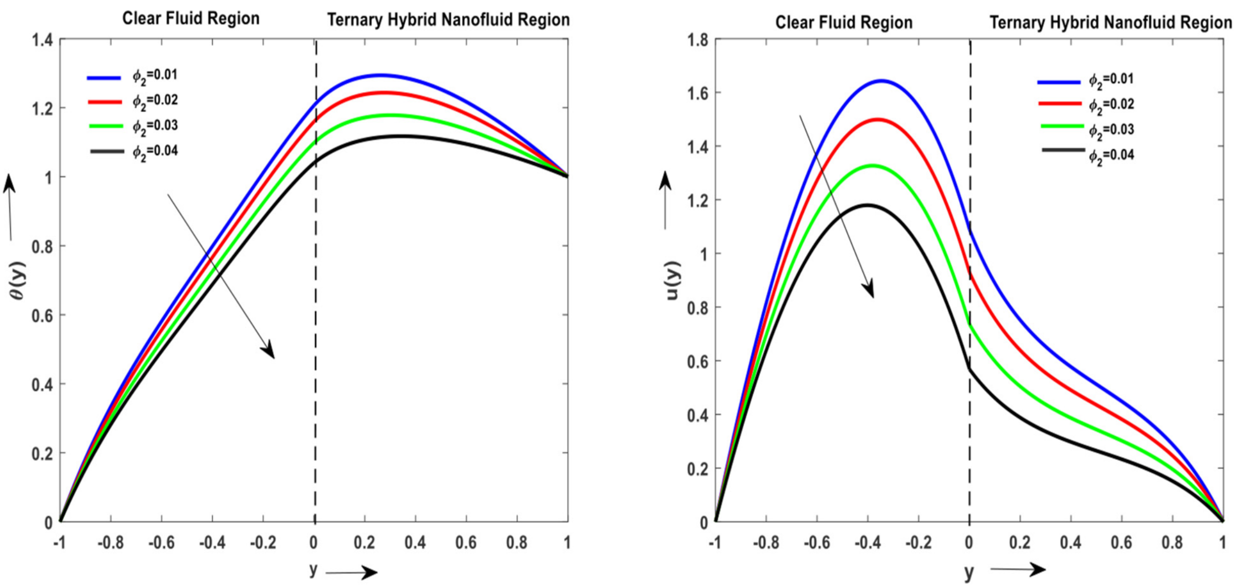

Figure 7. The impact of ϕ_2 on $\theta(y)$ and $u(y)$.

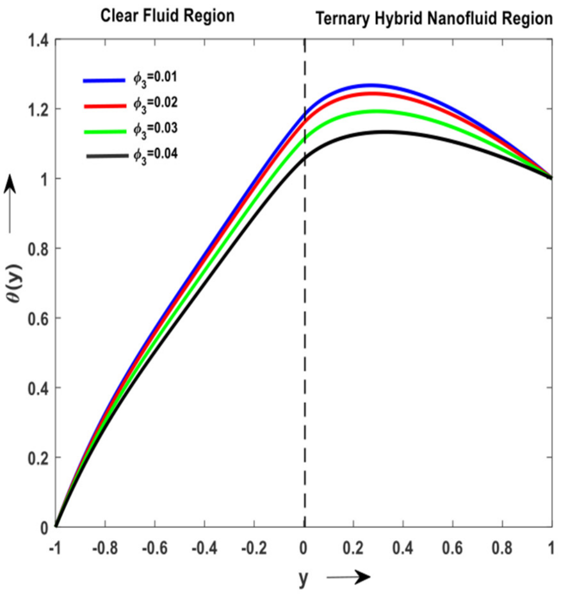

Figure 8. The impact of ϕ_3 on $\theta(y)$ and $u(y)$.

Figure 9 shows the impact of Grt and Br on Nu at both plates. According to Figure 9, Nu at $y = -1$ increases with Grt and Br. The colour transition in the graphs indicates that maximum Grt and Br values result in the highest heat transmission. Figure 9 illustrates how Grt and Br affect the Nusselt number at $y = 1$. Physically, rising levels of Grt and Br strengthen buoyancy and kinetic energy from viscous dissipation, strengthening convectional heat transmission. The fluid consequently acquires heat from the plate. The rate of heat transmission is considered to be at its maximum at $y = -1$.

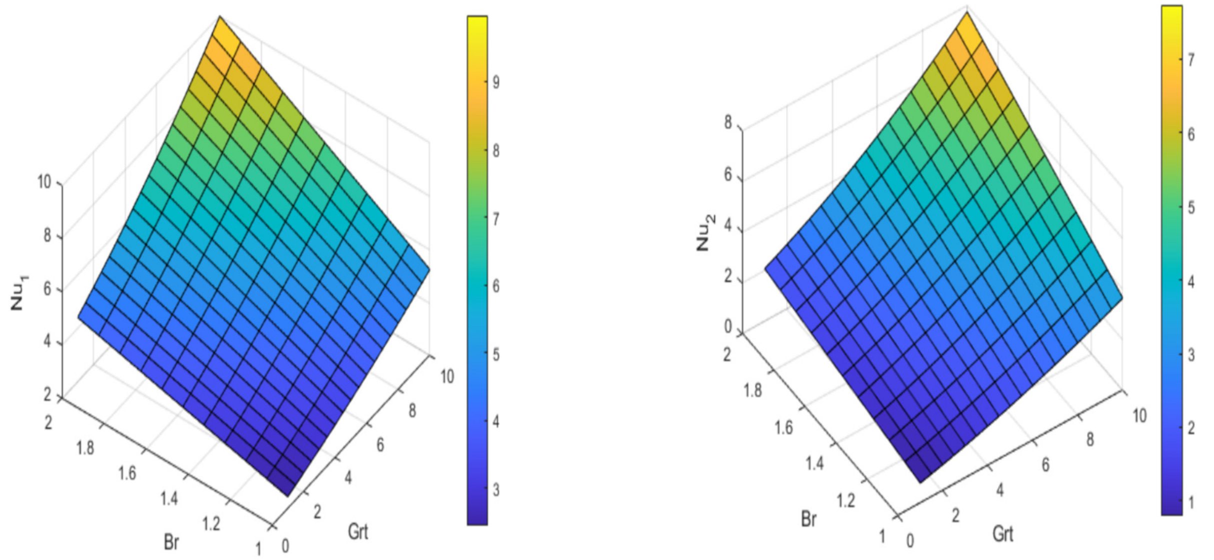

Figure 9. The effect of Grt and Br on Nusselt number at $y = -1$ and $y = 1$.

The effects of σ and R on Nu at both plates are depicted in Figure 10. Figure 10 in particular shows that as σ and R rise, Nu rises. On the other side, as permeability enhances, there is an increase in friction between the particles, which raises the temperature. In contrast, as R increases, the fluid's thermal conductivity decreases. These two elements have an impact on Nu. So, compared to Figure 9, Nu is lower.

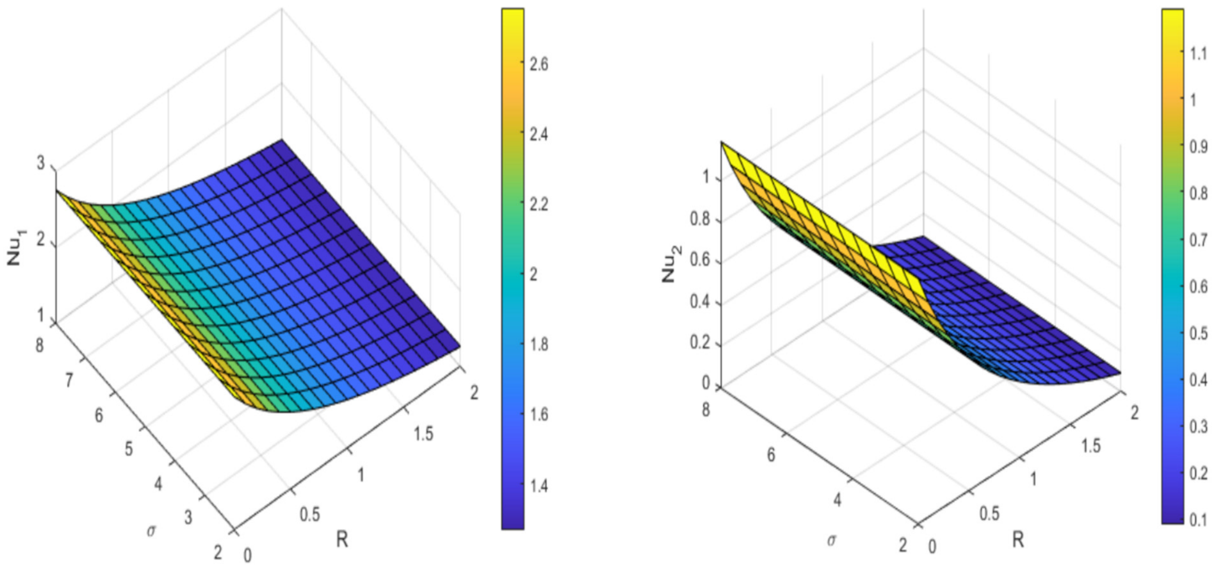

Figure 10. The effect of σ and R on Nusselt number at $y = -1$ and $y = 1$.

Grt and Br have an impact on C_f at both plates, as shown in Figure 11. The shear stress rises at both plates as Grt and Br rise. The impact of Grt and Br is seen in Figure 11 at $y = -1$. The variation in C_f rises with increasing buoyancy forces. Viscous dissipation also affects skin friction in addition to the preceding. Hence, the resistance to the laminar flow will build up, resulting in the upsurge of the skin friction of the fluid. An identical phenomenon is observed at $y = 1$ (elucidated in Figure 11). The resistance to the flow is higher at $y = 1$ than at $y = -1$.

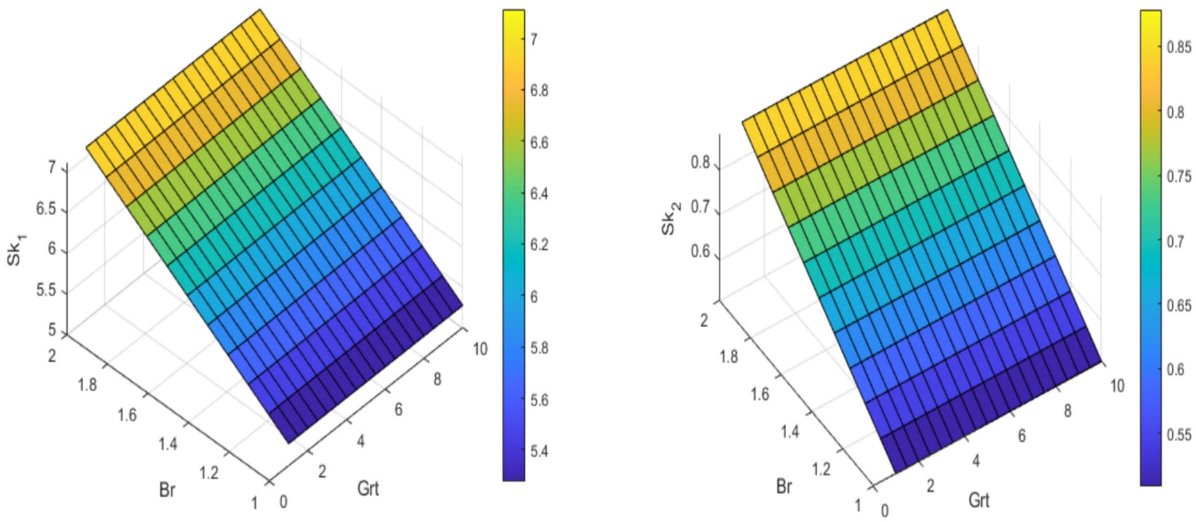

Figure 11. The effect of Grt and Br on skin friction coefficient at $y = -1$ and $y = 1$.

The effects of σ and R on C_f at both plates are displayed in Figure 12. Skin friction decreases at both plates as the porosity parameter and the thermal radiation parameter rise. At $y = -1$ and $y = 1$, the reduction rate is high and low, respectively. Physically, as σ increases, the resistance the increases. On the other hand, a rise in the values of R reduces the shear rate.

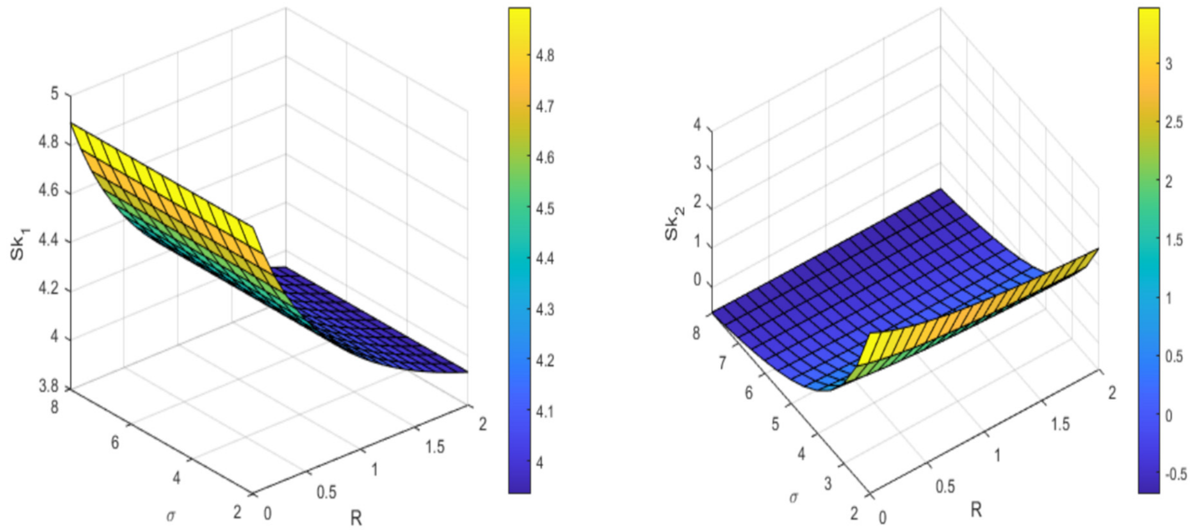

Figure 12. The skin friction coefficient profiles against σ and R at $y = -1$ and $y = 1$.

Table 3 provides the percentage enhancement of the Nusselt number for various nanoparticle concentrations suspended in PEG–water. The effect of shape factors on the rate of heat transmission is explored in this research. From the table, we can observe that in the absence of platelet-shaped MgO nanoparticles, 1% of spherical-shaped ZrO_2 as well as CNTs in PEG–Water show a promising enhancement of 42% at $y = -1$ and 753% at $y = 1$. This is the novelty of the study. The observed enhancements in heat transfer could be used to boost the performance of heat exchangers, thermal management in electronics, solar collectors, and the oil recovery industries. As the concentration of nanoparticles is decreased from 5% to 1%, the thermal performance of the base fluid is improved by 10% to 42%. The optimum rate of heat transfer is reached at 1% nanoparticle concentration. As $y = -1$ corresponds to the clear fluid region and $y = 1$ corresponds to the ternary hybrid nanofluid region, the enhancement of the heat transfer is significantly higher at $y = 1$, that is 753.82%.

Table 3. Effect of ϕ_1, ϕ_2 and ϕ_3 on Nusselt number.

ϕ_1 Spherical	ϕ_2 Platelet	ϕ_3 Cylindrical	Nusselt Number		Percentage Enhancement	
			Nu_1	Nu_2	Nu_1 (%)	Nu_2 (%)
0	0.05	0.05	1.5193	0.1007	-	-
0.05	0	0.05	1.6776	0.2863	10.42	184.31
0.05	0.05	0	1.6426	0.2478	8.11	146.07
0	0.04	0.04	1.5896	0.1887	4.63	87.39
0.04	0	0.04	1.7731	0.4003	16.71	297.51
0.04	0.04	0	1.7188	0.3408	13.13	238.4
0	0.03	0.03	1.6909	0.3126	11.29	210.42
0.03	0	0.03	1.8917	0.5395	24.51	435.75
0.03	0.03	0	1.8165	0.4580	19.56	354.81
0	0.02	0.02	1.8361	0.4854	20.85	382.02
0.02	0	0.02	2.0290	0.6990	33.55	594.14
0.02	0.02	0	1.9404	0.6041	27.72	499.90
0	0.01	0.01	2.0346	0.7158	33.92	610.82
0.01	0.01	0	2.0932	0.7815	37.77	676.06
0.01	0	0.01	2.1671	0.8598	42.64	753.82

Table 4 also shows the effects of related variables on the E and Q through the channel. As Grt and Br increase, the total heat flow and the volume flow across the channel also improve. This is due to the fact that increasing buoyant force and kinetic energy cause the fluid to flow more quickly, accelerating heat transfer from the wall to the fluid and ultimately increasing the quantity of heat transferred to the fluid in the channel. But a reverse phenomenon is observed for a rise in the values of R, ϕ_2, ϕ_3, and σ. The total heat flow added to the flow reduces.

Table 4. The impact of pertinent parameters on total heat and volume flow.

		Total Heat Flow (E)	**Total Volume Flow (Q)**
Grt	1	0.68231	1.003
	5	1.3387	1.5446
	10	3.0018	2.6068
Br	0.1	0.6218	1.2406
	0.5	1.3387	1.5446
	1	2.5564	1.9245
ϕ_1	0.02	1.3387	1.5446
	0.04	1.4314	1.6153
	0.06	1.4597	1.6343
ϕ_2	0.02	1.3387	1.5446
	0.04	0.8454	1.1277
	0.06	0.5722	0.86752
ϕ_3	0.02	1.3387	1.5446
	0.04	0.9001	1.1759
	0.06	0.5902	0.8850
R	0.2	1.6942	1.6677
	0.4	1.4871	1.5975
	0.6	1.3387	1.5446
σ	2	3.8869	3.1685
	4	1.3387	1.5446
	6	0.7492	1.0715

5. Validation of Results

It is interesting to note that the governing Equations (1)–(4) in this research are reduced to those of a viscous fluid by taking into account $\phi_1 = \phi_2 = \phi_3 = 0$. Our results have been compared to those of Malashetty et al. [51] to verify the validity of the present research. In the absence of radiation parameter and $\phi_1 = \phi_2 = \phi_3 = 0$, $P_1 = P = -5$, σ, subscripts $f = 1$, $thnf = 2$, there will be no difference between the governing Equations (5)–(10) of Malashetty et al. [51] for Region II and Region I and the governing Equations (1)–(5) of the present study for Region I and Region II. Additionally, the impact of Grt on temperature shown in Figure 13 for the aforesaid assumptions and $\sigma = 5$ is the same as that shown in Figure 6 by Malashetty et al. [51]. The temperature profiles of the present study and that of Malashetty et al. [51] are of similar pattern but not exactly same. This difference is due to the inclination of the channel. The present study considers the angle of inclination as $\cos 30^0$, while Malashetty et al. [51] use $\sin 30^0$. In the presence of above-mentioned effects, the fluid's temperature in the ternary hybrid nanofluid region is increased by approximately 200%, which is clearly shown in the Figure 2.

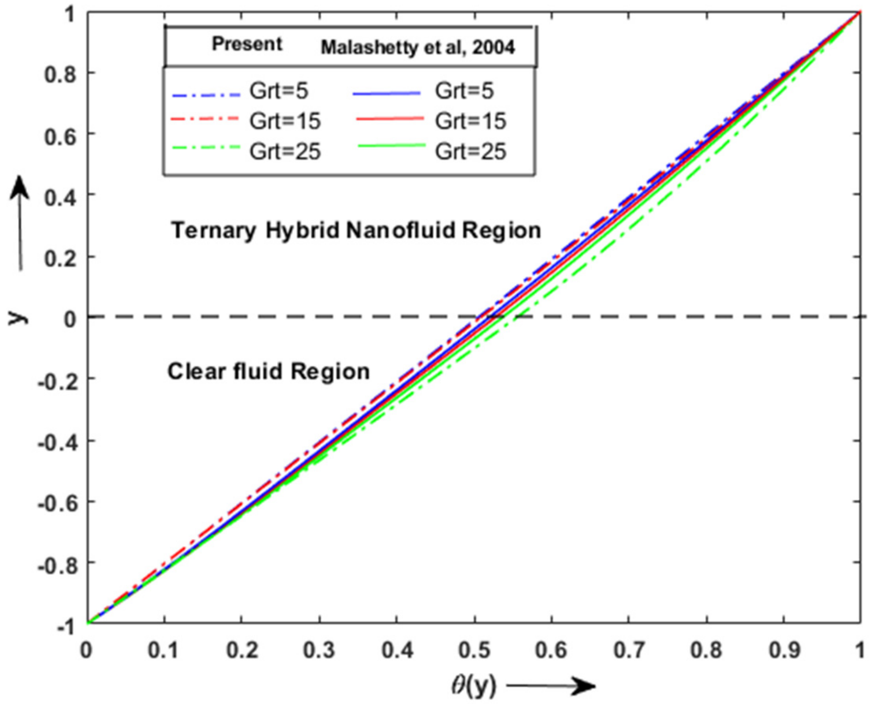

Figure 13. The impact of Grt on $\theta(y)$.

6. Conclusions

In this article, we look at ternary hybrid nanofluids and their potential for solving real-world problems. According to the experimental findings, hybrid nanofluids transmit heat at a pace that is faster than unitary nanofluids. In light of the foregoing, this paper explores the effect on thermal efficiency of a PEG–water-based ternary nanofluid containing nanoparticles with spherical, platelet, and cylindrical shapes. In PEG–Water, we have combined spherical ZrO_2, platelet-shaped MgO, and cylindrical SWCNTs. The aforementioned combination is taken into account in a two-phase inclined channel with thermal radiation, viscous, and Darcy dissipation. Thermophysical characteristics of a ternary hybrid nanofluid are defined using a mixture model. Ternary nanofluids are modelled using the Maxwell-Garnet thermoelectric model and the Einstein-Batchelor viscosity equation. The impact of modifications to derived quantities and non-dimensional parameters on flow features is examined using visualisations and tabular data. The outcomes are briefly summarised in this section.

- The region of ternary hybrid nanofluids exhibits improved heat transmission relative to the region of clear fluids.
- Thermal buoyancy forces and kinetic energy generated by viscous dissipation are responsible for enhancing fluid temperature, but the porosity and radiation parameters reverse this tendency.
- Due to buoyancy and viscous forces, the velocity of clear fluid increases more than that of ternary hybrid nanofluids. Conversely, the fluid's velocity is lowered by thermal radiation and porosity factors.
- An increase in the volume of ZrO_2 nanoparticles enhances fluid temperature and velocity. In contrast, a rise in the volume fraction of MgO and CNTs reduces fluid temperature and velocity due to the nature of the materials.
- In comparison to plate $y = 1$, plate $y = -1$ shows the highest rate of heat transmission. The heat from the plate is consequently transferred to the fluid.
- There is more resistance to flow with the fluid with the plate $y = -1$ than with the plate $y = 1$.

- A decrease in nanoparticle volume fraction from 5% to 1% with different combinations increased the heat transfer rate from 10% to 42% at $y = -1$. But heat transfer enhancement of 753.82% is observed at $y = 1$.
- With increasing Grt and Br, the total heat rate and volumetric flow rate added to the flow increase.
- The ternary nanofluids can increase the heat transfer potential.
- The aforementioned conclusions have some theoretically guiding implications for oil recovery systems, heat exchangers, thermal energy storage, nuclear reactor cooling, and high-temperature industrial processes.

This field has the potential to contribute to more efficient and sustainable energy and heat transport systems as it develops. Extensive practical studies are required to validate the theoretical model and numerical simulations. Furthermore, the characterization of nanofluids and porous media will shed light on the potential for heat transmission. It demonstrates to the scientific and industrial communities that ternary nanofluids have greater heat transfer capability than traditional fluids.

Author Contributions: Methodology, P.S.; Software, B.N.H. and A.V.; Investigation, S.V.K.V.; Data curation, S.A.; Writing—original draft, K.M.P.; Writing—review & editing, N.A.S. All authors have read and agreed to the published version of the manuscript.

Funding: This project was supported by Researchers Supporting Project number (RSPD2023R909), King Saud University, Riyadh, Saudi Arabia.

Data Availability Statement: The authors confirm that the data supporting the findings of this study are available within the article.

Acknowledgments: This work was supported by the research seed grant ref no.: RU: EST:MT:2022/3 funded by REVA University. This project was supported by Researchers Supporting Project number (RSPD2023R909), King Saud University, Riyadh, Saudi Arabia.

Conflicts of Interest: The authors declare no conflict of interest.

Nomenclature

Grt—Thermal Grashof number	R—Radiation parameter
Br—Brinkman number	g—Acceleration due to gravity $\left[ms^{-2}\right]$
k—Thermal conductivity $[W/mK]$	$u\prime$—Velocity of the fluid $\left[ms^{-1}\right]$
q_r—Radiative heat flux	m—Shape factor
K—Permeability	C_p–Specific heat $\left[Jkg^{-1}K^{-1}\right]$
P—Pressure $\left[kg\ m^{-1}s^{-2}\right]$	PEG—Polyethylene glycol-water
ZrO_2—Zirconium oxide	MgO—Magnesium oxide
Nu—Nusselt number	C_f—Skin friction
$SWCNT$—Single-walled carbon nanotube	
Greek Symbols	
σ—Porosity Parameter	ϕ_1—volume fraction of ZrO_2
ϕ_2—volume fraction of MgO	ϕ_3—volume fraction of SWCNT
β—Thermal expansion coefficient $\left[K^{-1}\right]$	η—Sphericity
σ_s—Stefan-Boltzmann constant	k_a—the mean absorption coefficient.
μ—Viscosity $\left[kgm^{-1}s^{-1}\right]$	ρ—Density $\left[kg/m^3\right]$
Subscripts:	
f—Fluid	p-Nanoparticle
nf—Nanofluid	bf—Base fluid
$nf1$—ZrO–PEG Nanofluid	$nf2$—MgO–PEG Nanofluid
$nf3$—SWCNT–PEG Nanofluid	$thnf$—Ternary hybrid nanofluid

Appendix A

$d_1 = \frac{K_{thnf}}{K_f}$	$L_6 = \frac{4L_2^2+6L_1c_{11}}{12}$
$b_3 = \frac{1}{1+d_1}$	$L_7 = \frac{12L_1L_2}{20}$
$b_1 = b_2 = b_4 = \frac{d_1}{1+d_1}$	$L_8 = \frac{4c_{11}L_2}{6}$
$L_1 = \frac{Grtb_1}{6}$	$L_9 = \frac{c_{11}^2}{2}$
$L_2 = -\frac{Grtb_2}{2} + \frac{P}{2}$	$L_{10} = -\frac{L_3}{\sigma^2}$
$L_3 = -aGrtb_3$	$L_{11} = -\frac{L_4}{\sigma^2}$
$L_4 = -aGrtb_4 - P_1$	$L_{12} = \left(c_{21}^2 + c_{22}^2\right)\sigma^2$
$L_5 = \frac{9L_1^2}{30}$	$L_{13} = 4\sigma^2 c_{21}c_{22}$
$L_{14} = 2c_{21}L_{10}\sigma^2$	$L_{15} = 2c_{22}L_{10}\sigma^2$
$L_{16} = 2\sigma^2 L_{11}c_{21} + 2\sigma c_{22}L_{10}$	$L_{17} = 2\sigma^2 L_{11}c_{22} + 2\sigma c_{21}L_{10}$
$L_{18} = L_{10}^2$	$L_{19} = 2L_{10}L_{11}$
$L_{20} = \frac{L_{12}}{4\sigma^2}$	$L_{21} = \frac{L_{13}}{4\sigma^2}$
$L_{22} = \frac{L_{14}\sigma}{\sigma^3}$	$L_{23} = \frac{L_{15}}{\sigma^2}$
$L_{24} = \frac{L_{16}}{\sigma^2}$	$L_{25} = \frac{L_{17}}{\sigma^2}$
$L_{26} = \frac{L_{18}}{12}$	$L_{27} = \frac{L_{19}}{9}$
$L_{28} = \frac{L_{10}^2+L_{11}^2}{2}$	$L_{29} = \frac{L_{20}}{3\sigma^2}$
$L_{30} = \frac{L_{21}}{3\sigma^2}$	$L_{31} = \frac{L_{22}}{4\sigma}$
$L_{32} = -\frac{L_{22}}{4\sigma^2}$	$L_{33} = \frac{L_{23}}{4\sigma}$
$L_{34} = -\frac{L_{23}}{4\sigma^2}$	$L_{35} = \frac{L_{24}}{2\sigma}$
$L_{36} = \frac{L_{25}}{2\sigma}$	$L_{37} = \frac{L_5}{56}$
$L_{38} = \frac{L_6}{42}$	$L_{39} = \frac{L_7}{30}$
$L_{40} = -\frac{L_8}{20}$	$L_{41} = \frac{L_9}{12}$
$L_{42} = \frac{c_{21}}{6}$	$L_{43} = \frac{c_{22}}{2}$

References

1. Choi, S.U.S.; Eastman, J.A. *Enhancing Thermal Conductivity of Fluids with Nanoparticles*; Argonne National Lab. (ANL): Argonne, IL, USA, 1995.
2. Turcu, R.; Darabont, A.L.; Nan, A.; Aldea, N.; Macovei, D.; Bica, D.; Vekas, L.; Pana, O.; Soran, M.L.; Koos, A.A. New Polypyrrole-Multiwall Carbon Nanotubes Hybrid Materials. *J. Optoelectron. Adv. Mater.* **2006**, *8*, 643–647.
3. Jana, S.; Salehi-Khojin, A.; Zhong, W.-H. Enhancement of Fluid Thermal Conductivity by the Addition of Single and Hybrid Nano-Additives. *Thermochim. Acta* **2007**, *462*, 45–55. [CrossRef]
4. Suresh, S.; Venkitaraj, K.P.; Selvakumar, P.; Chandrasekar, M. Synthesis of Al_2O_3–Cu/Water Hybrid Nanofluids Using Two Step Method and Its Thermo Physical Properties. Colloids Surf. *Physicochem. Eng. Asp.* **2011**, *388*, 41–48. [CrossRef]
5. Chen, X.; Jian, Y. Entropy Generation Minimization Analysis of Two Immiscible Fluids. *Int. J. Therm. Sci.* **2022**, *171*, 107210. [CrossRef]
6. Hisham, M.D.; Rauf, A.; Vieru, D.; Awan, A.U. Analytical and Semi-Analytical Solutions to Flows of Two Immiscible Maxwell Fluids between Moving Plates. *Chin. J. Phys.* **2018**, *56*, 3020–3032. [CrossRef]
7. Yadav, P.K.; Kumar, A. An Inclined Magnetic Field Effect on Entropy Production of Non-Miscible Newtonian and Micropolar Fluid in a Rectangular Conduit. *Int. Commun. Heat Mass Transf.* **2021**, *124*, 105266. [CrossRef]
8. Mallikarjuna, B.; Bhatta, S.S.; Ramprasad, S. Velocity and Thermal Slip Effects on MHD Convective Radiative Two-Phase Flows in an Asymmetric Non-Uniform Channel. *Propuls. Power Res.* **2021**, *10*, 169–179. [CrossRef]
9. Zeeshan, A.; Shehzad, N.; Atif, M.; Ellahi, R.; Sait, S.M. Electromagnetic Flow of SWCNT/MWCNT Suspensions in Two Immiscible Water-and Engine-Oil-Based Newtonian Fluids through Porous Media. *Symmetry* **2022**, *14*, 406. [CrossRef]
10. Umavathi, J.C.; Bég, O.A. Effects of Thermophysical Properties on Heat Transfer at the Interface of Two Immisicible Fluids in a Vertical Duct: Numerical Study. *Int. J. Heat Mass Transf.* **2020**, *154*, 119613. [CrossRef]

11. Dogonchi, A.S.; Chamkha, A.J.; Seyyedi, S.M.; Ganji, D.D. Radiative Nanofluid Flow and Heat Transfer between Parallel Disks with Penetrable and Stretchable Walls Considering Cattaneo–Christov Heat Flux Model. *Heat Transfer—Asian Res.* **2018**, *47*, 735–753. [CrossRef]
12. Rahim, T.; Hasnain, J.; Abid, N.; Abbas, Z. Entropy Generation for Mixed Convection Flow in Vertical Annulus with Two Regions Hydromagnetic Viscous and Cu-Ag Water Hybrid Nanofluid through Porous Zone: A Comparative Numerical Study. *Propuls. Power Res.* **2022**, *11*, 401–415. [CrossRef]
13. Yaseen, M.; Rawat, S.K.; Shafiq, A.; Kumar, M.; Nonlaopon, K. Analysis of Heat Transfer of Mono and Hybrid Nanofluid Flow between Two Parallel Plates in a Darcy Porous Medium with Thermal Radiation and Heat Generation/Absorption. *Symmetry* **2022**, *14*, 1943. [CrossRef]
14. Pattnaik, P.K.; Pattnaik, J.R.; Mishra, S.R.; Nisar, K.S. Variation of the Shape of Fe 3 O 4-Nanoparticles on the Heat Transfer Phenomenon with the Inclusion of Thermal Radiation. *J. Therm. Anal. Calorim.* **2021**, 1–12.
15. Khan, U.; Zaib, A.; Ishak, A.; Sherif, E.-S.M.; Waini, I.; Chu, Y.-M.; Pop, I. Radiative Mixed Convective Flow Induced by Hybrid Nanofluid over a Porous Vertical Cylinder in a Porous Media with Irregular Heat Sink/Source. *Case Stud. Therm. Eng.* **2022**, *30*, 101711. [CrossRef]
16. Upreti, H.; Pandey, A.K.; Kumar, M. Unsteady Squeezing Flow of Magnetic Hybrid Nanofluids within Parallel Plates and Entropy Generation. *Heat Transf.* **2021**, *50*, 105–125. [CrossRef]
17. Masood, S.; Farooq, M. Influence of Thermal Stratification and Thermal Radiation on Graphene Oxide-Ag/H 2 O Hybrid Nanofluid. *J. Therm. Anal. Calorim.* **2021**, *143*, 1361–1370. [CrossRef]
18. Xiong, P.-Y.; Nazeer, M.; Hussain, F.; Khan, M.I.; Saleem, A.; Qayyum, S.; Chu, Y.-M. Two-Phase Flow of Couple Stress Fluid Thermally Effected Slip Boundary Conditions: Numerical Analysis with Variable Liquids Properties. *Alex. Eng. J.* **2022**, *61*, 3821–3830. [CrossRef]
19. Ge-JiLe, H.; Nazeer, M.; Hussain, F.; Khan, M.I.; Saleem, A.; Siddique, I. Two-Phase Flow of MHD Jeffrey Fluid with the Suspension of Tiny Metallic Particles Incorporated with Viscous Dissipation and Porous Medium. *Adv. Mech. Eng.* **2021**, *13*, 16878140211005960. [CrossRef]
20. Wakif, A.; Boulahia, Z.; Ali, F.; Eid, M.R.; Sehaqui, R. Numerical Analysis of the Unsteady Natural Convection MHD Couette Nanofluid Flow in the Presence of Thermal Radiation Using Single and Two-Phase Nanofluid Models for Cu–Water Nanofluids. *Int. J. Appl. Comput. Math.* **2018**, *4*, 81. [CrossRef]
21. Xiong, Q.; Tayebi, T.; Izadi, M.; Siddiqui, A.A.; Ambreen, T.; Li, L.K. Numerical Analysis of Porous Flat Plate Solar Collector under Thermal Radiation and Hybrid Nanoparticles Using Two-Phase Model. *Sustain. Energy Technol. Assess.* **2021**, *47*, 101404. [CrossRef]
22. Al-Hossainy, A.F.; Eid, M.R. Combined Experimental Thin Films, TDDFT-DFT Theoretical Method, and Spin Effect on [PEG-H_2O/ZrO_2 + MgO] h Hybrid Nanofluid Flow with Higher Chemical Rate. *Surf. Interfaces* **2021**, *23*, 100971. [CrossRef]
23. Al-Hossainy, A.F.; Eid, M.R. Combined Theoretical and Experimental DFT-TDDFT and Thermal Characteristics of 3-D Flow in Rotating Tube of [PEG+ H_2O/SiO_2-Fe_3O_4] C Hybrid Nanofluid to Enhancing Oil Extraction. *Waves Random Complex Media* **2021**, 1–26. [CrossRef]
24. Babu, M.J.; Rao, Y.S.; Kumar, A.S.; Raju, C.S.K.; Shehzad, S.A.; Ambreen, T.; Shah, N.A. Squeezed Flow of Polyethylene Glycol and Water Based Hybrid Nanofluid over a Magnetized Sensor Surface: A Statistical Approach. *Int. Commun. Heat Mass Transf.* **2022**, *135*, 106136. [CrossRef]
25. Murshid, N.; Mulki, H.; Abu-Samha, M.; Owhaib, W.; Raju, S.S.K.; Raju, C.S.; JayachandraBabu, M.; Homod, R.Z.; Al-Kouz, W. Entropy Generation and Statistical Analysis of MHD Hybrid Nanofluid Unsteady Squeezing Flow between Two Parallel Rotating Plates with Activation Energy. *Nanomaterials* **2022**, *12*, 2381. [CrossRef]
26. Ahmad, S.; Nadeem, S. Thermal Analysis in Buoyancy Driven Flow of Hybrid Nanofluid Subject to Thermal Radiation. *Int. J. Ambient Energy* **2022**, *43*, 3868–3876. [CrossRef]
27. Rana, P.; Kumar, A. Nonlinear Buoyancy Driven Flow of Hybrid Nanoliquid Past a Spinning Cylinder with Quadratic Thermal Radiation. *Int. Commun. Heat Mass Transf.* **2022**, *139*, 106439. [CrossRef]
28. Adun, H.; Kavaz, D.; Dagbasi, M. Review of Ternary Hybrid Nanofluid: Synthesis, Stability, Thermophysical Properties, Heat Transfer Applications, and Environmental Effects. *J. Clean. Prod.* **2021**, *328*, 129525. [CrossRef]
29. Shamshuddin, M.D.; Akkurt, N.; Saeed, A.; Kumam, P. Radiation Mechanism on Dissipative Ternary Hybrid Nanoliquid Flow through Rotating Disk Encountered by Hall Currents: HAM Solution. *Alex. Eng. J.* **2023**, *65*, 543–559. [CrossRef]
30. Younis, O.; Abderrahmane, A.; Hatami, M.; Mourad, A.; Kamel, G. Thermal Energy Storage Using Nano Phase Change Materials in Corrugated Plates Heat Exchangers with Different Geometries. *J. Energy Storage* **2022**, *55*, 105785. [CrossRef]
31. Abderrahmane, A.; Hatami, M.; Medebber, M.A.; Haroun, S.; Ahmed, S.E.; Mohammed, S. Non-Newtonian Nanofluid Natural Convective Heat Transfer in an Inclined Half-Annulus Porous Enclosure Using FEM. *Alex. Eng. J.* **2022**, *61*, 5441–5453. [CrossRef]
32. Ghadikolaei, S.S.; Hosseinzadeh, K.; Hatami, M.; Ganji, D.D.; Armin, M. Investigation for Squeezing Flow of Ethylene Glycol ($C_2H_6O_2$) Carbon Nanotubes (CNTs) in Rotating Stretching Channel with Nonlinear Thermal Radiation. *J. Mol. Liq.* **2018**, *263*, 10–21. [CrossRef]
33. Pavithra, K.M.; Hanumagowda, B.N.; Raju, S.S.K.; Varma, S.V.K.; Murshid, N.; Mulki, H.; Al-Kouz, W. Thermal Radiation and Mass Transfer Analysis in an Inclined Channel Flow of a Clear Viscous Fluid and H_2O/EG-Based Nanofluids through a Porous Medium. *Sustainability* **2023**, *15*, 4342. [CrossRef]

34. Pavithra, K.M.; Hanumagowda, B.N.; Varma, S.V.K.; Ahammad, N.A.; Raju, C.S.K.; Noeiaghdam, S. The Impacts of Shape Factors in a Chemically Reacting Two-Passage Vertical Channel Filled with Kerosene Based Graphene Oxide and MoS_2 Mixture in a Porous Medium. *Results Eng.* **2023**, *18*, 101050. [CrossRef]
35. Sarada, K.; Gamaoun, F.; Abdulrahman, A.; Paramesh, S.O.; Kumar, R.; Prasanna, G.D.; Gowda, R.P. Impact of Exponential Form of Internal Heat Generation on Water-Based Ternary Hybrid Nanofluid Flow by Capitalizing Non-Fourier Heat Flux Model. Case Stud. *Therm. Eng.* **2022**, *38*, 102332.
36. Bilal, M.; Ahmed, A.E.-S.; El-Nabulsi, R.A.; Ahammad, N.A.; Alharbi, K.A.M.; Elkotb, M.A.; Anukool, W.; SA, Z.A. Numerical Analysis of an Unsteady, Electroviscous, Ternary Hybrid Nanofluid Flow with Chemical Reaction and Activation Energy across Parallel Plates. *Micromachines* **2022**, *13*, 874. [CrossRef] [PubMed]
37. Sahoo, R.R. Heat Transfer and Second Law Characteristics of Radiator with Dissimilar Shape Nanoparticle-Based Ternary Hybrid Nanofluid. *J. Therm. Anal. Calorim.* **2021**, *146*, 827–839. [CrossRef]
38. Sahu, M.; Sarkar, J. Steady-State Energetic and Exergetic Performances of Single-Phase Natural Circulation Loop with Hybrid Nanofluids. *J. Heat Transf.* **2019**, *141*, 082401. [CrossRef]
39. Arif, M.; Kumam, P.; Kumam, W.; Mostafa, Z. Heat Transfer Analysis of Radiator Using Different Shaped Nanoparticles Water-Based Ternary Hybrid Nanofluid with Applications: A Fractional Model. *Case Stud. Therm. Eng.* **2022**, *31*, 101837. [CrossRef]
40. Keerthana, L.; Sakthivel, C.; Prabha, I. MgO-ZrO_2 Mixed Nanocomposites: Fabrication Methods and Applications. *Mater. Today Sustain.* **2019**, *3*, 100007. [CrossRef]
41. Matizamhuka, W.R. Spark Plasma Sintering (SPS)-an Advanced Sintering Technique for Structural Nanocomposite Materials. *J. S. Afr. Inst. Min. Metall.* **2016**, *116*, 1171–1180. [CrossRef]
42. Chamkha, A.J.; Miroshnichenko, I.V.; Sheremet, M.A. Numerical Analysis of Unsteady Conjugate Natural Convection of Hybrid Water-Based Nanofluid in a Semicircular Cavity. *J. Therm. Sci. Eng. Appl.* **2017**, *9*, 041004. [CrossRef]
43. Tiwari, R.K.; Das, M.K. Heat Transfer Augmentation in a Two-Sided Lid-Driven Differentially Heated Square Cavity Utilizing Nanofluids. *Int. J. Heat Mass Transf.* **2007**, *50*, 2002–2018. [CrossRef]
44. Timofeeva, E.V.; Routbort, J.L.; Singh, D. Particle Shape Effects on Thermophysical Properties of Alumina Nanofluids. *J. Appl. Phys.* **2009**, 106. [CrossRef]
45. Vold, R.D.; Vold, M.J. *Colloid and Interface Chemistry*; Addison-Wesley: Boston, MA, USA, 1983.
46. Rosseland, S. *Theoretical Astrophysics*; Oxford University Press: London, UK, 1936.
47. Siegel, R.; Howell, J.R. *Thermal Radiation Heat Transfer*, 3rd ed.; Hemisphere: Washington, WA, USA, 1936.
48. Malashetty, M.S.; Umavathi, J.C.; Kumar, J.P. Magnetoconvection of Two-Immiscible Fluids in Vertical Enclosure. *Heat Mass Transf.* **2006**, *42*, 977–993. [CrossRef]
49. Umavathi, J.C.; Hemavathi, K. Flow and Heat Transfer of Composite Porous Medium Saturated with Nanofluid. *Propuls. Power Res.* **2019**, *8*, 173–181. [CrossRef]
50. Das, S.; Guchhait, S.K.; Jana, R.N. Radiation Effects on Unsteady MHD Free Convective Couette Flow of Heat Generation/Absorbing Fluid. *Int. J. Comput. Appl.* **2012**, *39*, 42–51. [CrossRef]
51. Malashetty, M.S.; Umavathi, J.C.; Prathap Kumar, J. Two Fluid Flow and Heat Transfer in an Inclined Channel Containing Porous and Fluid Layer. *Heat Mass Transf.* **2004**, *40*, 871–876. [CrossRef]